©2014 Society of Economic Geologists, Inc.
*Economic Geology*, v. 109, pp. 1787–1799

# *GEOLOGY, GEOCHEMISTRY, AND GENESIS OF TUNGSTEN-TIN DEPOSITS IN THE BAIGANHU DISTRICT, NORTHERN KUNLUN BELT, NORTHWESTERN CHINA*

Yongbao Gao,[1,†] Wenyuan Li,[1] Zhiming Li,[1] Jian Wang,[2] Keiko Hattori,[3] Zhaowei Zhang,[1] and Jianzhen Geng[4]

[1] *MLR Key Laboratory of Genesis and Exploration of Magmatic Ore Deposits, Xi'an Institute of Geology and Mineral Resources, Xi'an, Shaanxi, 710054, P. R. China*

[2] *College of Earth Sciences, Jilin University, Changchun, Jilin, 130061, P. R. China*

[3] *Department of Earth Sciences, University of Ottawa, Ottawa, Canada K1N 6N5*

[4] *Tianjin Institute of Geology and Mineral Resources, Tianjin, 300170, P. R. China*

## Abstract

Mineralized occurrences in the Baiganhu district were discovered in 2002 after extensive exploration in the eastern Kunlun domain in the Kunlun terrane. Tungsten-Sn deposits in the area contain total resources of 174, 913 metric tons (t) of $WO_3$ and 79, 091 t of Sn, which makes the Baiganhu field a new large W-Sn metallogenic province after the Nanling region of southern China. The W-Sn mineralization in the Baiganhu field is spatially associated with monzogranite that yielded a $^{238}U$-$^{206}Pb$ zircon age of 430.5 ± 1.2 Ma ($n$ = 25). Cassiterite yielded a $^{206}Pb/^{207}Pb$-$^{238}U/^{207}Pb$ isochron age of 427 ± 13 Ma ($n$ = 32), which confirms a close relationship of the early Silurian intrusion and the W-Sn mineralization. The timing of the mineralization indicates another important W-Sn metallogenic event in China in addition to the period of Late Jurassic (from 160–150 Ma) in the Nanling region.

The mineralization is divided into three stages: (I) scheelite-bearing skarn stage, (II) wolframite- and scheelite-bearing greisenization stage, and (III) wolframite- and cassiterite-bearing quartz-veining stage. Quartz in the wolframite- and cassiterite-bearing quartz veins shows two types of fluid inclusions: liquid-rich two-phase aqueous inclusions and $CO_2$-rich and $CH_4$-bearing three-phase inclusions. Inclusions have medium salinity (10–14 wt % NaCl equiv), low density (0.60–1.06 g/cm$^3$), and moderate homogenization temperatures (240°–270°C). The $CO_2$ phase in three-phase inclusions shows a large variation from 10 to 70 vol %, which is attributed to immiscible separation of a $CO_2$-rich phase from saline aqueous fluids. The immiscible separation likely contributed to the mineralization in quartz veins. The $\delta^{18}O_{H_2O}$ values of the mineralizing fluids calculated from quartz and $\delta D$ of inclusion fluids in quartz vary from +4.5 to +6.4 ‰ and –65 to –43‰, respectively, supporting that the mineralizing fluids originated from the parental magmas.

## Introduction

Tungsten-tin mineralization is closely associated with granitic intrusions. China is the world's leading producer of W and Sn (Carlin, 2013; Shedd, 2013), and the metals are mostly mined in the Nanling region in southern China (Fig. 1) where the W-Sn deposits are associated with granitic rocks of 160 to 150 Ma (Mao et al., 2007; Feng et al., 2011). Therefore, the major metallogenic epoch of W-Sn mineralization is considered to be Jurassic in age. The Kunlun orogenic terrane on the north margin of the Tibetan plateau contains abundant granitic intrusions of Paleozoic to Mesozoic age and some are accompanied by quartz veining and greisenization. The occurrence of these granitic rocks prompted exploration for W and Sn deposits in the area beginning in 2000 and resulted in the discovery of a W-Sn deposit in the Baiganhu area in 2002, a deposit in the Jialesai area in 2006, and many potential areas in the eastern Kunlun domain of the belt. Resources at the Keke-Kaerde deposit in the Baiganhu field are 140,437 metric tons (t) of $WO_3$ and 77,651 t of Sn at cutoff grades of 0.15% $WO_3$ and 0.1% Sn, respectively. The total indicated resources in the area as of 2013 are 174,913 t of $WO_3$ and 79,091 t of Sn, and these numbers are expected to increase with ongoing exploration. These figures have already made the Baiganhu area a new W-Sn metallogenic province.

† Corresponding author: e-mail, gaoyongbao2006@126.com

The Keke-Kaerde deposit is the first economic W-Sn mineralization found on the Tibetan plateau; thus, the documentation of the deposit is important. Previous work related to the area hosting the W-Sn mineralization includes a regional metallogenetic study (Li et al., 2006; Song et al., 2010), the geologic setting of the deposit (Li et al., 2006), and the geochemical characteristics and genetic model of the mineralization (Liu et al., 2007). This paper documents the U-Pb ages of zircon grains of monzogranite that is closely associated with the W-Sn mineralization, a U-Pb isochron age of cassiterite, fluid inclusion heating-cooling data, and H and O isotope compositions of mineralizing fluids and discusses the nature of the hydrothermal fluids. The information is useful in exploration for W-Sn deposits in the region and elsewhere.

## Geologic Setting

The Kunlun orogenic terrane is a major tectono-magmatic terrane on the northern margin of the Tibetan plateau (Fig. 1), bounded by the Arkin orogenic belt and the Qaidam basin to the north and the Bayankala fold belt to the south (Fig. 1B). The terrane has been subject to a complex tectonic history involving rifting to form the Proto-Tethys Ocean in the Late Proterozoic, closure of the ocean in the early Paleozoic (Li et al., 2008), and accretion during subduction of the Paleo-Tethys oceanic lithosphere from the south. Based on the tectonic history, the Kunlun orogenic terrane is divided into three belts: northern Kunlun (Qimantage)

0361-0128/14/4249/1787-13

*Submitted: August 21, 2013*
*Accepted: January 16, 2014*

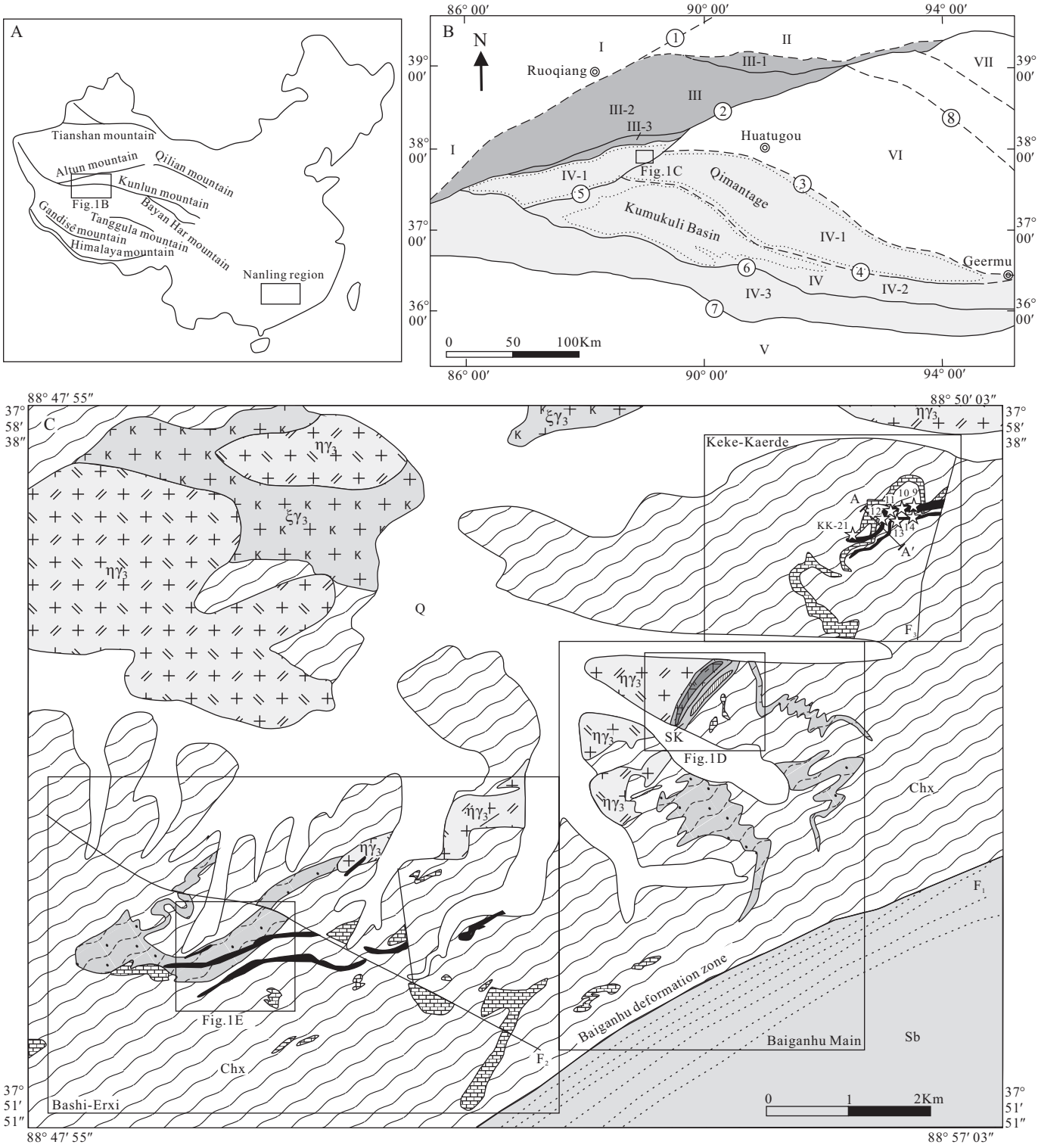


FIG. 1. A. Location of the study area and mountain ranges (thick lines). B. A simplified regional tectonic map (modified after Li et al., 2008). I = Tarim basin; II = north Arkin-Dunhuang block; III = Arkin orogenic belt (dark gray): III-1 = Hongliugou-Lapeiquan ophiolitic mélange belt, III-2 = Mid-Arkin massif, III-3 = Apa-Mangya early Paleozoic ophiolitic mélange belt; IV = east Kunlun domain (light gray): IV-1 = northern Kunlun (Qimantage) early Paleozoic arc, IV-2 = Mid-Kunlun microcontinent, IV-3 = southern Kunlun accretionary complex; V = Bayankala fold belt; VI = Qaidam basin; VII = Qilian orogenic belt. Thick lines are fault and deformation zones, and dashed lines are inferred structures; ① = north Arkin deformation zone, ② = south Arkin deformation zone, ③ = north Kunlun fault, ④ = Heishan-Nalinggele fault, ⑤ = Baiganhu deformation zone, ⑥ = Mid-Kunlun fault, ⑦ = south Kunlun deformation zone, ⑧ = fault defining the northern boundary of the Qaidam basin. Areas enclosed by dotted lines are Qimantage and Kumukuli basin. C. Geologic map showing three W-Sn deposits of the Baiganhu district (modified after a map provided by the Institute of Geologic Survey of Jilin Province).

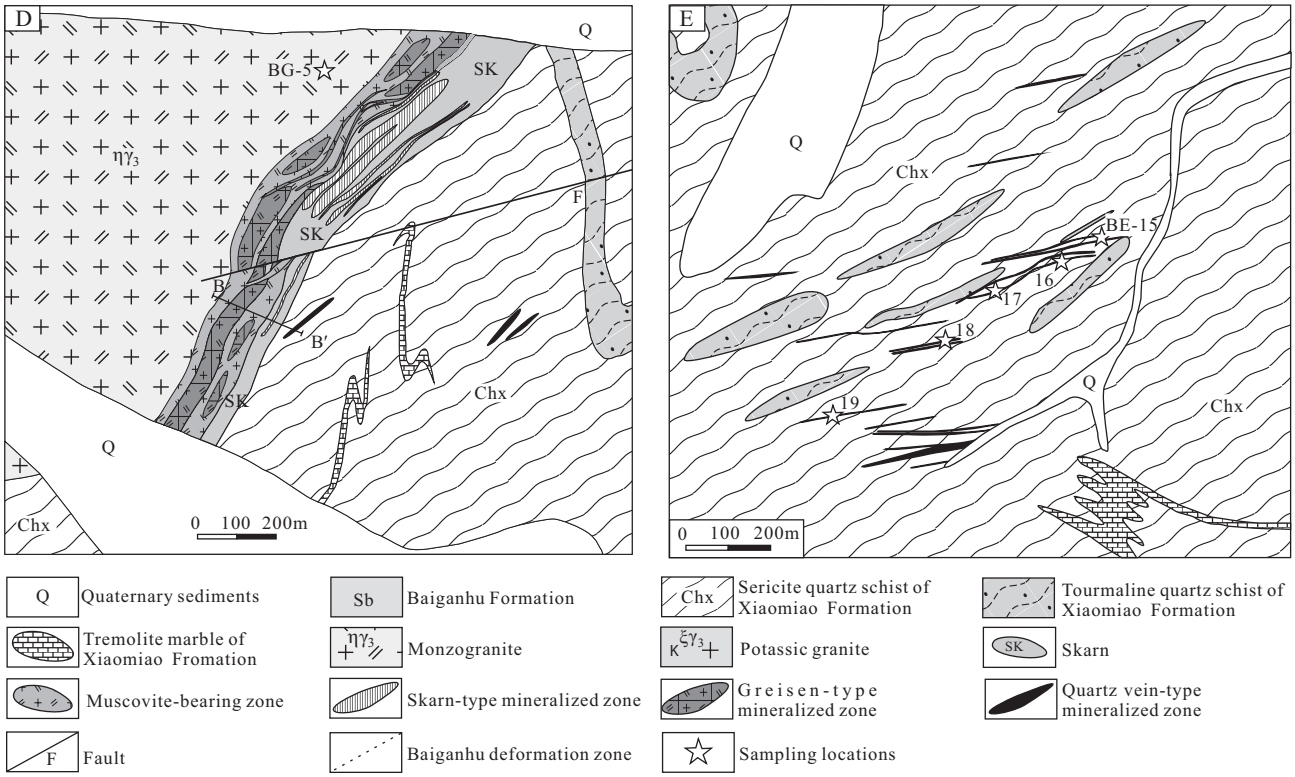


FIG. 1. *(Cont.)* D. Detailed geologic map showing the Baiganhu Main W-Sn deposit (modified after a map provided by the Institute of Geologic Survey of Jilin Province). E. Detailed geologic map showing the Bashi-Erxi W-Sn deposit (modified after a map provided by the Institute of Geologic Survey of Jilin Province). Skarns are composed of tremolite, diopside, muscovite, and quartz. Occurrences are defined by cutoff grades of 0.15 wt % $WO_3$ and 0.1 wt % Sn. Sampling locations are shown with stars and sample numbers are depicted next to the symbols. Samples collected in the Keke-Kaerde deposit, Baiganhu Main deposit, and Bashi-Erxi deposit start with KK, BG, and BE, respectively.

belt, Mid-Kunlun microcontinent, and southern Kunlun accretionary complex (Fig. 1B). The northern Kunlun belt represents a continental arc complex of early Paleozoic age formed during the north-dipping subduction of the Proto-Tethys Ocean. It contains abundant calc-alkaline volcanic rocks and intrusions (Mo et al., 2007). The northern Kunlun belt is further divided into the east Kunlun and west Kunlun domains by the Altyn Tagh fault (Yang et al., 1996; Fig. 1B) and the study area is across the boundary between the east and west Kunlun domains in the northern Kunlun belt (Fig. 1B). During subduction of the Proto-Tethys ocean, the Kunlun orogenic terrane was in a compressive regime, but the cessation of the subduction in the Silurian resulted in local extension allowing the deposition of molasse-type sediments (the Qimulafu formation) and bimodal volcanism (the Maoniushan formation; Pan et al., 1994). This extension also led to intrusion of voluminous anorogenic granites (Jiang et al., 2008). It was followed by the development of mafic-ultramafic plutons and the deposition of voluminous turbidites in the Galesai-Yaziquan-Shizigou area, central northern Kunlun belt (Li et al., 2003).

Subduction of the Paleo-Tethys during the late Paleozoic to the early Mesozoic produced granitic intrusions throughout the Kunlun orogenic terrane and the southern Kunlun accretionary complex. Eventual closure of the Paleo-Tethys formed the A'nyemaqen ophiolite belt in the southern margin of the accretional complex (Yang et al., 2009). Some of the epizonal granitic intrusions are accompanied by porphyry-, skarn-, and vein-type Cu, Au, Fe, Pb, Zn, and Mo mineralization (Gao et al., 2010).

The Baiganhu district is situated west of the Baiganhu deformation zone in the Qimantage area, in the northern Kunlun (Qimantage) early Paleozoic arc of the east Kunlun domain (Fig. 1B). The Qimantage area is bounded by the Qimantage Mountains to the north and the Cenozoic Kumukuli basin to the south (Mo et al., 2007; Li et al., 2008; Gao et al., 2010). The Qimantage Mountains are composed mainly of intermediate to felsic intrusions.

The Qimantage area is characterized by a group of NE- and NW-trending structures. Field investigations by Li et al. (2008) recognized two NE-trending deformation zones (the south Arkin deformation zone and the Baiganhu deformation zone) and three NW-trending fault systems (the north Kunlun fault, Heishan-Nalinggele fault, and Mid-Kunlun fault). The NE-trending Baiganhu deformation zone is the main structure in the study area (Fig. 1C) ranging from 2.5 to 5 km wide, with dips 70° to 80° to the SE, and a sinistral sense of movement. Brittle fractures are also well developed in the study area, and most of them are structures related to the Baiganhu deformation zone, mostly SE dipping, parallel to or oblique (intersection angle of 40°–50°) to the Baiganhu deformation zone. The deformation zone is accompanied by folds, most of which are tight folds with NE-trending axes. Late open folds are characterized by broad, angled noses.

Influenced by Cenozoic collision of Indian and Asian plates, the northward fold-thrust belt occurred along the north Kunlun fault, and the south Arkin deformation zone was active as a sinistral strike slip fault (Li et al., 2008).

## Geology of Mineral Deposits

The Baiganhu district is at elevations ranging from 4,100 to 4,400 m above sea level, located ~90 km southwest of the town of Huatugou (Fig. 1B). It may be accessed by gravel roads from the town. The area is underlain by the Mesoproterozoic Xiaomiao formation and the Silurian Baiganhu formation. The Xiaomiao formation is mostly comprised of two-mica quartz schist, amphibolite, biotitie-bearing plagiogneiss, and quartzite. The protoliths may be siliclastic and carbonate sedimentary rocks with minor volcanic rocks. The area has abundant granitic intrusions of varying size, including monzogranite and potassic granite, whic are accompanied by contact metamorphic aureoles in siliciclastic rocks and skarns in carbonate rocks of the Xiaomiao formation. Contact relationships show the intrusion of potassic granite into monzogranite (Fig. 1C). The W-Sn deposits with economic grades are all associated with the monzogranite (Fig. 1C).

### *Occurrence of deposits*

As of 2013, a total of 76 discrete mineral occurrences have been discovered in the Baiganhu W-Sn field and can be grouped into three main clusters: Bashi-Erxi, Baiganhu Main, and Keke-Kaerde (Fig. 1C). The W-Sn deposits formed through three principal events:

The first event is early crystallization of tremolite, diopside, and scheelite in tremolite-diopside skarns during the skarnization along the contacts between monzogranite intrusions and the Xiaomiao formation (Fig. 1D). The skarns contain minor biotite, chlorite, and quartz. Diopside is an early mineral formed at high temperatures and is mostly replaced by tremolite. Biotite is partially altered to chlorite. The tremolite-diopside skarn at the Baiganhu Main deposit is about 900 m long, 50 to 120 m wide (Fig. 1D), and about 50 m in vertical thickness (Fig. 2). Carbonate rocks in the host Xiaomiao formation close to skarns are extensively recrystallized to form marble. Siliclastic rocks of the Xiaomiao formation are altered to form sericite-quartz schist.

The second event is the development of a greisen-type deposit, where quartz, muscovite, tourmaline, fluorite, wolframite, and scheelite crystallized in the upper part and wall rocks of monzogranite intrusions (Figs. 1D, 2, 3). In this greisenization event, plagioclase and K-feldspar are replaced by muscovite and tourmaline. Fluorite is locally common, along with muscovite, and it replaces plagioclase and K-feldspar. The host rocks are silicified and chloritized.

The third event formed W- and Sn-bearing quartz-veins in the Xiaomiao formation and muscovite-bearing zone of monzogranite (Figs. 1D, E, 3). Crosscutting relationships clearly indicate that the veining took place after greisenization. The veins are composed of quartz, wolframite, cassiterite, and minor chlorite, and scheelite. The wall rocks of the veins are chloritized.

The Basi-Erxi deposit contains 45 economic occurrences of W-Sn deposits defined by cutoff grades of 0.15 wt % $WO_3$ and 0.1 wt % Sn. The entire occurrences are 200 to 720 m in length and 1.15 to 22.5 m in width. The deposits form quartz veins in monzogranites and occur in skarns and sericite-quartz schist of the Xiaomiao formation. The Baiganhu Main deposit contains the total six economic-grade skarn-type deposits along the contacts between monzogranite intrusions and marble, and two greisen-type deposits in the muscovite-bearing zone of monzogranite intrusions. The skarn-type deposits are 180 to 800 m in length and 1.66 to 13.3 m in width. The Keke-Kaerde deposit contains 23 occurrences of economic deposits, which are closely associated with a concealed monzogranite (Fig. 3). Six out of the 23 occurrences are entirely concealed with no apparent surface expression and were identified by drilling. There are three styles of economic mineral deposits: deposits hosted by quartz veins at shallow depths, skarn-type deposits along the contacts of the intrusion and marble, and greisen-type deposits in the uppermost part of the monzogranite.

### *Granitic intrusions and alteration*

The area contains abundant granitic intrusions with a total exposed area of more than 30 km² (Fig. 1C). Similar granitic

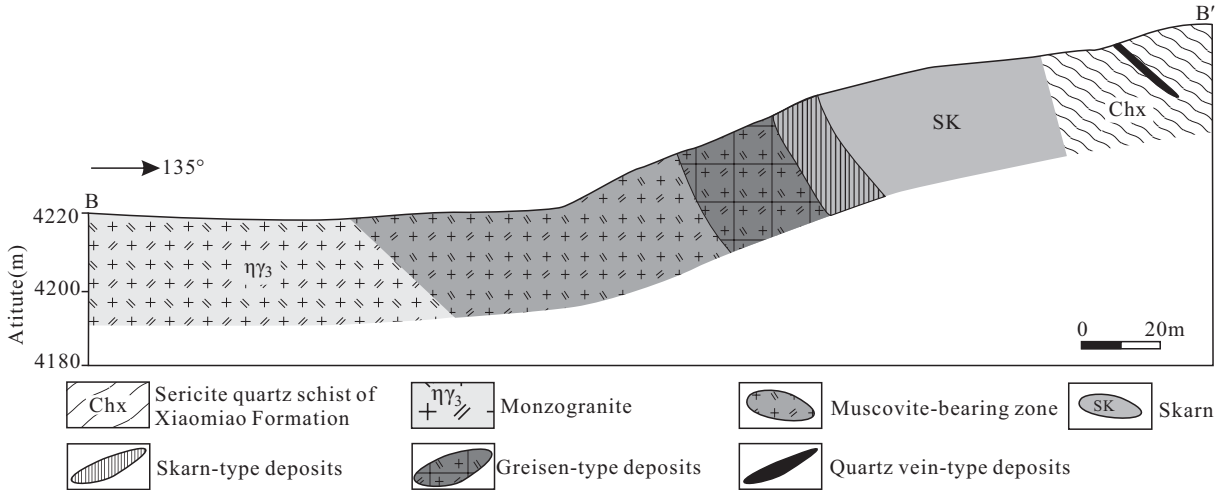


FIG. 2. Simplified cross section along B-B' of Figure 1D, showing the W-Sn mineralization in the Baiganhu Main deposit (modified after a map provided by Institute of Geologic Survey of Jilin Province).

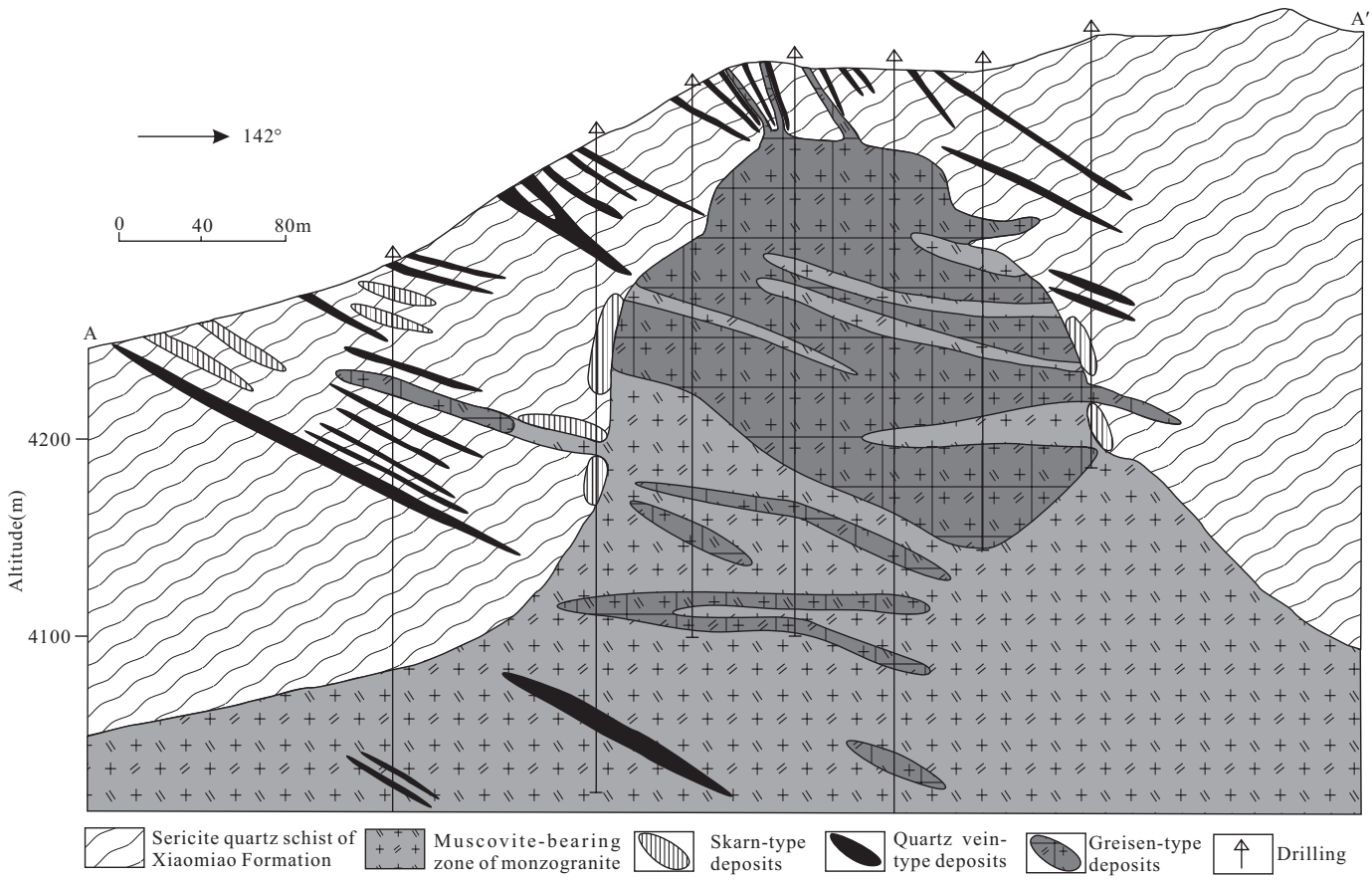


FIG. 3. Simplified cross section along A-A′ of Figure 1C, showing the W-Sn mineralization in the Keke-Kaerde deposit (modified after a map provided by Institute of Geologic Survey of Jilin Province).

intrusions form a batholith to the north of the Keke-Kaerde deposit and stocks in the Bashi-Erxi and Baiganhu Main deposits (Fig. 1C). They are monzogranite and coarse-grained potassic granite with the former closely related to the W-Sn mineralization. Alteration includes greisenization and silicification. Greisenization resulted in an increase in quartz and muscovite and a decrease in feldspars.

The unaltered monzogranites in the Baiganhu Main deposit are gray to light-red in color (Fig. 4A), with a subhedral granular texture. The main minerals are K-feldspar (>10 mm, 35–40 vol %), plagioclase (25–30%), quartz (25–30 vol %), and biotite (<10 vol %; Fig. 4B). Plagioclase forms euhedral platy crystals with minor kaolinization and sericitization. K-feldspar occurs as irregular xenomorphic granular shapes and is composed mainly of microcline with minor perthite. Accessory minerals include zircon, apatite, and titanite.

The muscovite-bearing zone has been formed by parially greisenization of monzogranites (Figs. 1D, 2, 3). In the Keke-Kaerde deposit, the rocks in the muscovite-bearing zone are gray in color on unweathered surfaces (Fig. 4C), subhedral fine grained, and consist mainly of granular quartz (0.5–1.2 mm, 40–45 vol %), plagioclase (up to 35 vol %), muscovite (0.2–0.4 × 0.4–0.8 mm, 15–~18 vol %), and K-feldspar (0.3 mm, up to 3 vol %; Fig. 4D). The plagioclase has subhedral or granular-shapes (0.2 × 0.3–0.4 × 0.8 mm).

*Types of deposits*

There are three types of economic W-Sn mineralization in the area: skarn, greisens, and quartz veins. Skarn-type mineralization shows granular blastic texture and occurs in tremolite-diopside skarns of the Xiaomiao formation and endoskarn in monzogranite (Fig. 4C). The main economic mineral is scheelite, which is accompanied by tremolite, diopside, muscovite, and quartz. Cassiterite is not observed in this type of deposits. The second type is greisen-type mineralization, which forms veins (0.5–1.1 m in width), and lenses occurring in the upper parts of a monzogranite intrusion (Fig. 3) and in the country rock (Fig. 4E). The mineralzation is medium to coarse grained and shows euhedral to subhedral granular texture. Economic minerals are mainly wolframite and scheelite that are accompanied by quartz, muscovite, fluorite, and tourmaline. The third type is quartz vein occurrences in the Xiaomiao formation and a muscovite-bearing zone of monzogranite (Figs. 2, 3). The width of the veins with economic metal grades ranges from 0.5 to 2.0 m. Tungsten- and tin-bearing quartz veins cut earlier formed W-bearing greisen veins (Fig. 4E). There are two stages of quartz veinning: E-W–trending, wolframite- and cassiterite-bearing quartz veins (0.5–1.0 m in width) and late chalcopyrite-bearing NE-SW–trending quartz veins (0.1–0.2 m in width; Fig. 4F). Tungsten- and tin-bearing quartz veins contain wolframite, cassiterite (Fig. 4G), and minor scheelite

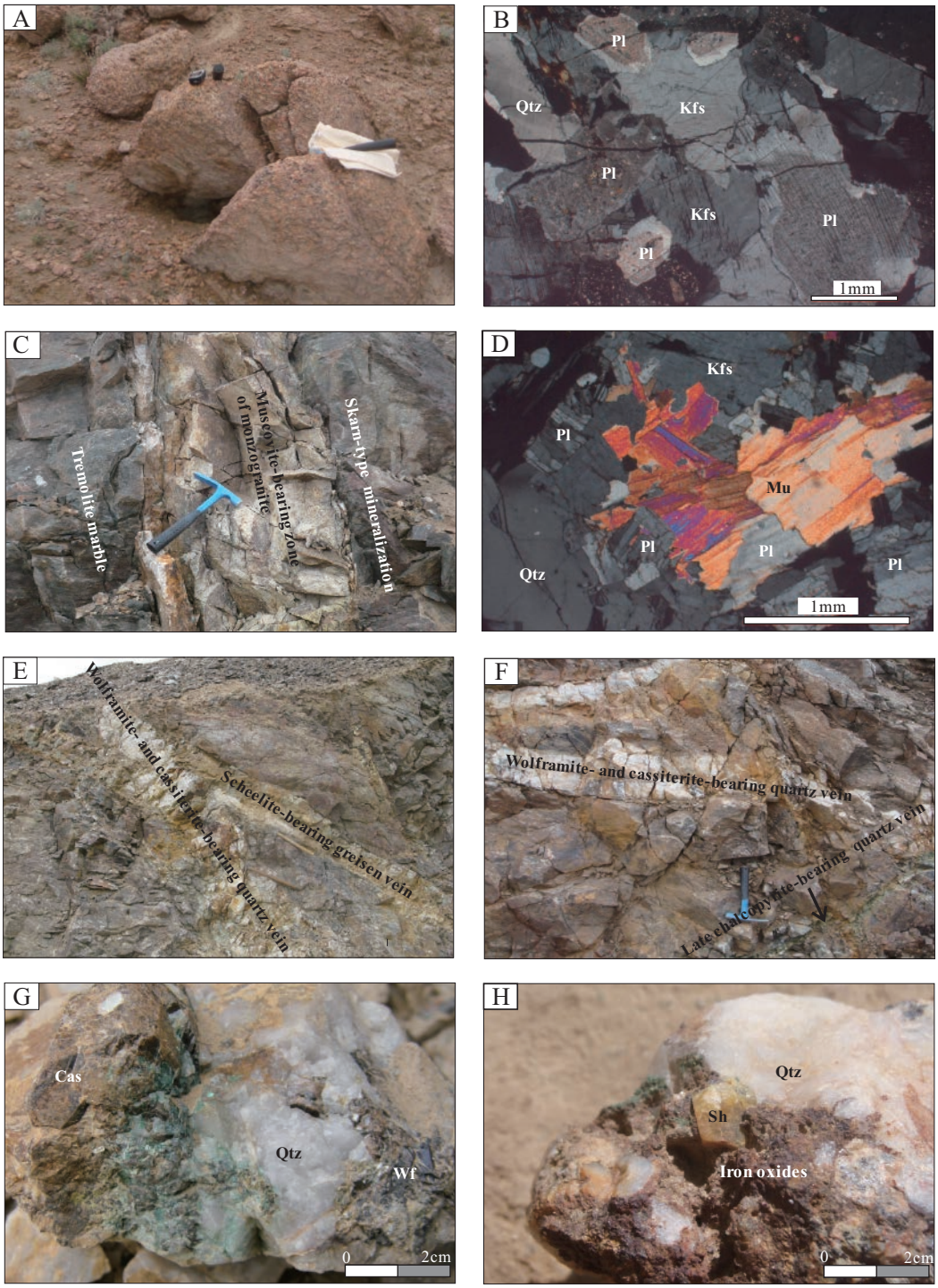


FIG. 4. A. Photograph showing the surface exposure of unaltered monzogranite in Baiganhu Main deposit at N37°58'38.6" and E88°55'38.9". B. Photomicrograph of unaltered monzogranite consisting of K-feldspar (Kfs), plagioclase (Pl), and quartz (Qtz). Plagioclase shows albite twins and is partially sericitized. C. Surface exposure of rocks in the muscovite-bearing zone of monzogranite and skarn-type mineralization along the contact between monzogranite and marble in the Xiaomiao formation in the Keke-Kaerde deposit at N37°57'33.6", E88°56'20.6". Scheelite occurs both in the tremolite-diopside skarn and greisen. D. Photomicrograph of rocks in the muscovite-bearing zone of monzogranite mainly consisting of quartz (Qtz), plagioclase (Pl), muscovite (Mu), and K-feldspar (Kfs). E. Photograph showing scheelite-bearing greisen vein was cut by a cassiterite- and wolframite-bearing quartz vein in the open pit of the Keke-Kaerde deposit at N37°57'34.7" and E88°56'22.8". Hammer = scale in the footwall of the greisen vein. F. Photograph showing that the wolframite- and cassiterite-bearing E-W–trending quartz vein was cut by late chalcopyrite-bearing NE-SW–trending quartz vein in the Keke-Kaerde deposit at N37°57'36.4"; E88°56'27.8". G. Photograph of a representative quartz vein-type mineralization where coarse crystalline cassiterite (Cas) and wolframite (Wf) occur in quartz from the Keke-Kaerde deposit. H. Photograph of coarse crystalline scheelite (Sh) in quartz vein-type deposit, and iron oxides from the Baiganhu Main deposit.

(Fig. 4H) and are hosted by monzogranite, skarns, and sericite-quartz schist of the Xiaomiao formation.

*Sequence of hydrothermal activity*

At least four stages of hydrothermal activity are recognized based on crosscutting relationships. Stage I formed scheelite-bearing skarns hosted near the contact between monzogranite and marble of the Xiaomiao formation; stage II produced greisen, scheelite, and wolframite; stage III is represented by wolframite- and cassiterite-bearing E-W–trending quartz veins; and stage IV is the formation of late chalcopyrite-bearing NE-SW–trending quartz veins along the Baiganhu deformation zone, which cut across the W-Sn-bearing quartz veins.

## Sample Description and Analytical Methods

*Sample description*

One unaltered monzogranite sample, BG-5, was selected for U-Pb dating of zircon grains. The sample was collected at 37°58'38.6" N and 88°55'38.9" E (Fig. 1D). The cassiterite grains were separated for U-Pb dating from sample KK-21 in a wolframite- and cassiterite-bearing E-W–trending quartz vein in sericite-quartz schist of the Xiaomiao formation in the Keke-Kaerde deposit (Fig. 1C). Samples used for fluid inclusion and H-O isotope analysis were collected from wolframite- and cassiterite-bearing E-W–trending quartz veins in the Keke-Kaerde deposit (samples KK-9–KK-14; Fig. 1C) and in the Bashi-Erxi deposit (samples BE-15–BE-19; Fig. 1E).

*Analytical methods*

Zircon grains were separated using an isodynamic magnetic separator and a heavy liquid. Zircons were handpicked utilizing a binocular microscope, mounted in Epoxy resin, and polished to have the centers of grains on the polished surface. Cathodoluminescence (CL) imaging of zircon was carried out in the State Key Laboratory of Continental Dynamics at the Northwest University in China, and U-Th-Pb analyses were carried out using a Thermo Fisher Neptune multicollector ICP-MS attached to an Excimer laser (LA-MC-ICP-MS) at the Institute of Mineral Resources, Chinese Academy of Geological Sciences, Beijing. U-Th-Pb isotope ratios were determined relative to the Plešovice zircon and GJ-1 zircon, and their concentrations were calibrated relative to the M127 reference zircon provided by Slama et al. (2008). The instrumental techniques are similar to those described by Hou et al. (2009). In all analyzed zircon grains, common Pb correction was not necessary due to very low counts of $^{204}$Pb and high $^{206}$Pb/$^{204}$Pb (>5,000). The analytical uncertainties are presented as $2\sigma$. Uncertainties in mean ages are quoted at the 95% confidence level. Off-line raw data selection, integration of background and analyte signals, time-drift correction, and quantitative calibration for U-Pb dating were performed by computer program ICPMSDataCal, described by Liu et al. (2010). Concordia diagrams and weighted mean calculations were made, using Isoplot/Ex_ver3 by Ludwig (2003).

In-situ U-Pb dating of cassiterite was performed using a Thermo-Fisher Scientific Neptune MC-ICP-MS coupled with a UP193FX Excimer laser (ESI) at the Tianjing Institute of Geology and Mineral Resources, following the procedures given by Yuan et al. (2011). The $^{204}$Pb signal was not precisely measured due to the very low ion signal and interference from small amounts of $^{204}$Hg in the Ar gas. $^{206}$Pb/$^{207}$Pb-$^{238}$U/$^{207}$Pb isochron was drawn using the Isoplot program of Ludwig (2003). The accuracy and precision of the in-situ LA-MC-ICP-MS U-Pb dating of cassiterite are similar to the results of conventional U-Pb dating on cassiterite by ID-TIMS as reported by Yuan et al. (2011).

Eleven doubly polished sections of 0.3- to 0.5-mm thickness were prepared for fluid inclusion petrography and microthermometry; microthermometric analysis utilizing a Linkam TMS 94 freezing-heating stage at the Xi'an Institute of Geology and Mineral Resources. The stage is monitored with a chromel-alumel thermocouple. Final ice-melting and $CO_2$ homogenization temperatures were recorded with an accuracy of ±0.2°C, clathrate-melting temperatures with uncertainty of ±0.5°C, and the homogenization temperatures with ±2°C. The components of fluid inclusions were analyzed under ambient conditions (23°C and 65% humidity) using inVia laser Raman microprobe at the Xi'an Institute of Geology and Mineral Resources. Analytical conditions are as follows: 514.5 nm $Ar^+$ laser, 30 mW laser power, a slit width of 20 $\mu$m, and exposure time 10 s.

Eleven quartz samples were selected for hydrogen and oxygen isotope measurements. Oxygen was liberated after reacting with $BrF_5$. For hydrogen isotope analysis of fluid inclusions, quartz samples were heated in vacuum at 600°C to decrepitate inclusions. The water was reacted with Zn at 400°C to convert to $H_2$ gas (Coleman et al., 1982), which was collected with activated charcoal at liquid $N_2$ temperatures and its isotope composition was determined with a Thermo-Finnigan MAT 253 mass spectrometer at the Beijing Research Institute of Uranium Geology, China. Analytical reproducibility in this study is ±0.2‰ both O and H isotopes.

## Results

*U-Pb dating of zircon*

Zircon grains are mostly euhedral to subhedral, and cathodoluminescence (CL) images in SEM show no evidence of inherited zircon. It is concluded that zircon grains likely formed from the monzogranite melt. The large light rose to transparent grains (>60 $\mu$m) showing long prismatic shapes were selected for U-Pb dating. They show oscillatory zoning with Th/U ratios of 0.35 to 0.69 (Fig. 5), which confirm their magmatic origin. Measurements of 27 spots for 25 grains have $^{238}$U-$^{206}$Pb ages ranging from 429.3 ± 3.4 to 430.9 ± 3.4 Ma with the weighted mean value of 430.5 ± 1.2 Ma (MSWD = 0.0111; Table 1, Fig. 6). The data all plot on the Concordia curve or very close to the curve, suggesting no loss or addition of Pb. The age is considered to represent the solidification age of monzogranite in the Baiganhu W-Sn district.

*Geochronology of cassiterite*

Cassiterite grains used for the analysis are dark brown to translucent in thin sections and have rounded subhedral shapes. A large range in $^{206}$Pb/$^{207}$Pb ratios from 32 cassiterite grains provides a reliable $^{206}$Pb/$^{207}$Pb-$^{238}$U/$^{207}$Pb isochron age of 427 ± 13 Ma (95% confidence level, MSWD = 5.3, Fig. 7; Table 2). The age is identical to that of the monzogranite within uncertainty.

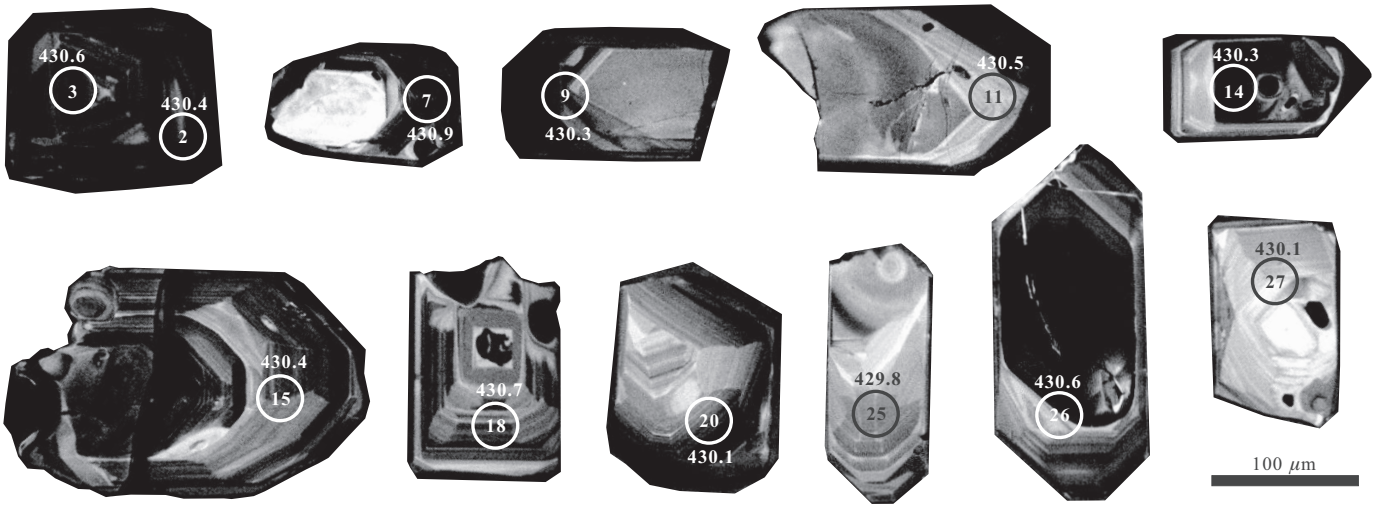


FIG. 5. Representative CL images of zircon from monzogranites (sample BG-5) from the Baiganhu Main deposit. The sample location is shown in Figure 1D. Circles are areas analyzed for U-Pb dating. The numbers in circles represent the analysis numbers in Table 1.

*Fluid inclusions*

Type I, liquid-rich two-phase inclusions, vary in size (5–15 $\mu$m) and shape (irregular or negative crystals; Fig. 8A). The volume of vapor is generally low, 5 to 15%. Laser-Raman analysis indicates that the liquid is mainly $H_2O$, whereas the vapor phase contains minor $CO_2$ and $CH_4$. Homogenization temperatures to liquid range from 129° to 343°C ($n$ = 51) with an average of 235°C and a median of 240°C (Fig. 9A); their ice-melting points and salinities are in the range of –0.5° to –17.8°C, which corresponds to 0.88 to ~20.8 wt % NaCl equiv (Fig. 9B), and their total densities range from 0.72 to 1.06 g/cm$^3$.

Type II inclusions have three phases consisting of vapor $CO_2$ ($V_{CO_2}$), liquid $CO_2$ ($L_{CO_2}$), and liquid $H_2O$ ($L_{H_2O}$) at room temperatures. They have various shapes (such as oval and quadrilateral) with the size of 5 to 25 $\mu$m. They commonly coexist with type I inclusions. The volume of $CO_2$ phase ($\varphi_{CO_2}$) varies from 10 to 70% of inclusions and these type II inclusions with varying $\varphi_{CO_2}$ spatially coexist (Fig. 8A). Raman spectra for the vapor phase indicate mainly $CO_2$ and $CH_4$, subordinate amounts of $H_2S$ and $N_2$ and minor $H_2$, and those for the liquid phase are mainly $H_2O$, with minor amounts of $CO_2$ and trace $CH_4$ and $H_2S$. The invariant point for type II three-phase inclusions ranges from –56.8° to –58.6°C ($n$ = 19). The value is lower than that for pure $CO_2$ (–56.6°C), suggesting the presence of $CH_4$, which is consistent with the Raman spectra. In type II fluid inclusions, $CO_2$ gas is homogenized to liquid $CO_2$ ($T_{h,CO_2}$) at –17.1° to ~27.3°C ($n$ =19). When $CO_2$ clathlate is formed, it melts at temperatures ranging from +0.3° to +6.5°C ($n$ =19). The data suggest that these $CO_2$-rich and $CH_4$-rich type II inclusions contain relatively low salinities, 6.6 to 15.2 wt % NaCl equiv (Fig.9B). During the heating of these fluid inclusions, they commonly decrepitated. Nondecrepitated inclusions yielded a total homogenization temperature range from 201° to 429°C with the median value of 270°C (mean value of 311°C). The density of type II inclusions is calculated to range from 0.60 to 0.91 g/cm$^3$, similar to that of type I inclusions.

One single-phase inclusion was observed in quartz. Raman analysis shows that it is pure $CH_4$ (Fig. 8B).

*Hydrogen and oxygen isotope compositions*

The values of $\delta^{18}O_{SMOW}$ for quartz from the wolframite- and cassiterite-bearing quartz veins range from +12.3 to +14.2‰

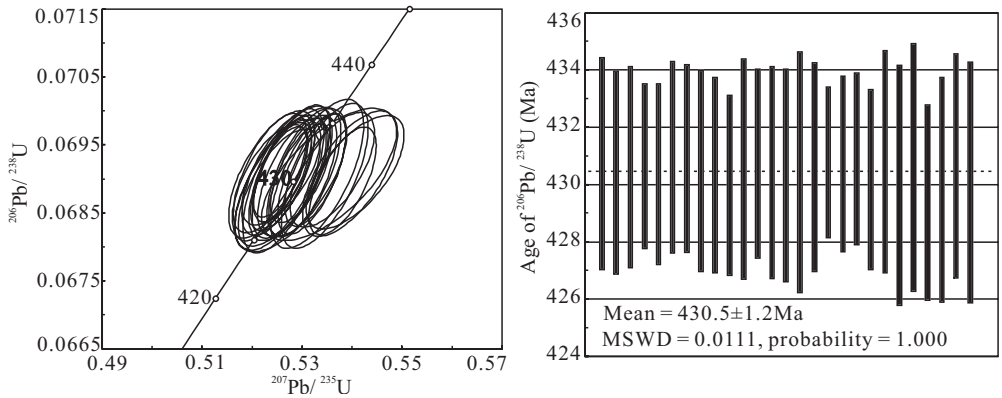


FIG. 6. LA-ICP-MS U-Pb concordia diagrams and histograms of weighted average ages for the analyzed zircon grains in monzogranite sample BG-5 from the Baiganhu Main deposit.

TABLE 1. U-Pb Dating Results of Zircon in Unaltered Monzogranite (sample BG-5) from the Baiganhu Main Deposit

| Analysis no.[1] | Pb (ppm) | Th (ppm) | U (ppm) | Th/U | $^{207}Pb/^{206}Pb$ Ratio | $^{207}Pb/^{206}Pb$ 1σ | $^{207}Pb/^{235}U$ Ratio | $^{207}Pb/^{235}U$ 1σ | $^{206}Pb/^{238}U$ Ratio | $^{206}Pb/^{238}U$ 1σ | $^{208}Pb/^{232}Th$ Ratio | $^{208}Pb/^{232}Th$ 1σ | $^{207}Pb/^{206}Pb$ Age | $^{207}Pb/^{206}Pb$ 1σ | $^{207}Pb/^{235}U$ Age | $^{207}Pb/^{235}U$ 1σ | $^{206}Pb/^{238}U$ Age | $^{206}Pb/^{238}U$ 1σ |
|---|---|---|---|---|---|---|---|---|---|---|---|---|---|---|---|---|---|---|
| 01 | 38.4 | 231.9 | 573.5 | 0.40 | 0.05572 | 0.00027 | 0.53039 | 0.00485 | 0.06910 | 0.00062 | 0.00387 | 0.00025 | 443 | 11.1 | 432.1 | 3.2 | 430.7 | 3.7 |
| 02 | 30.7 | 187.1 | 529.0 | 0.35 | 0.05577 | 0.00029 | 0.53010 | 0.00447 | 0.06904 | 0.00059 | 0.00368 | 0.00025 | 443 | 11.1 | 431.9 | 3.0 | 430.4 | 3.6 |
| 03 | 28.5 | 179.5 | 430.6 | 0.42 | 0.05596 | 0.00032 | 0.53197 | 0.00448 | 0.06908 | 0.00058 | 0.00387 | 0.00025 | 450 | 13.0 | 433.1 | 3.0 | 430.6 | 3.5 |
| 04 | 24.6 | 164.5 | 381.5 | 0.43 | 0.05567 | 0.00032 | 0.52975 | 0.00401 | 0.06908 | 0.00048 | 0.00369 | 0.00026 | 439 | 13.0 | 431.6 | 2.7 | 430.6 | 2.9 |
| 05 | 50.3 | 304.3 | 857.6 | 0.36 | 0.05525 | 0.00022 | 0.52582 | 0.00404 | 0.06903 | 0.00053 | 0.00350 | 0.00021 | 433 | 9.3 | 429.0 | 2.7 | 430.3 | 3.2 |
| 06 | 21.8 | 170.0 | 290.5 | 0.59 | 0.05622 | 0.00039 | 0.53607 | 0.00558 | 0.06913 | 0.00056 | 0.00376 | 0.00027 | 461 | 10.2 | 435.8 | 3.7 | 430.9 | 3.4 |
| 07 | 32.7 | 211.0 | 521.0 | 0.41 | 0.05595 | 0.00028 | 0.53269 | 0.00403 | 0.06913 | 0.00054 | 0.00351 | 0.00026 | 450 | 11.1 | 433.6 | 2.7 | 430.9 | 3.3 |
| 08 | 33.0 | 247.7 | 422.4 | 0.59 | 0.05517 | 0.00029 | 0.52523 | 0.00480 | 0.06905 | 0.00058 | 0.00342 | 0.00023 | 420 | 13.0 | 428.6 | 3.2 | 430.4 | 3.5 |
| 09 | 32.1 | 222.7 | 508.2 | 0.44 | 0.0555 | 0.00024 | 0.52817 | 0.00463 | 0.06903 | 0.00057 | 0.00303 | 0.0002 | 432 | 4.6 | 430.6 | 3.1 | 430.3 | 3.4 |
| 10 | 25.0 | 186.9 | 369.8 | 0.51 | 0.05664 | 0.00033 | 0.53812 | 0.00444 | 0.06897 | 0.00052 | 0.00307 | 0.00022 | 476 | 17.6 | 437.2 | 2.9 | 429.9 | 3.2 |
| 11 | 6.9 | 36.7 | 77.6 | 0.47 | 0.05648 | 0.00090 | 0.53544 | 0.00890 | 0.06906 | 0.00064 | 0.00961 | 0.00096 | 472 | 35.2 | 435.4 | 5.9 | 430.5 | 3.9 |
| 12 | 14.8 | 110.5 | 161.8 | 0.68 | 0.05693 | 0.00063 | 0.54063 | 0.00647 | 0.06910 | 0.00055 | 0.00410 | 0.00037 | 487 | 28.7 | 438.8 | 4.3 | 430.7 | 3.3 |
| 13 | 21.8 | 128.5 | 347.2 | 0.37 | 0.05470 | 0.00028 | 0.52157 | 0.00570 | 0.06904 | 0.00062 | 0.00381 | 0.00033 | 398 | 13.0 | 426.2 | 3.8 | 430.4 | 3.7 |
| 14 | 27.7 | 196.0 | 428.4 | 0.46 | 0.05504 | 0.00029 | 0.52350 | 0.00490 | 0.06903 | 0.00062 | 0.00305 | 0.00025 | 413 | 16.7 | 427.5 | 3.3 | 430.3 | 3.7 |
| 15 | 26.6 | 155.9 | 423.1 | 0.37 | 0.05614 | 0.00026 | 0.53452 | 0.00574 | 0.06905 | 0.00070 | 0.00363 | 0.00029 | 457 | 11.1 | 434.8 | 3.8 | 430.4 | 4.2 |
| 16 | 12.1 | 77.9 | 151.8 | 0.51 | 0.05688 | 0.00063 | 0.53959 | 0.00628 | 0.06908 | 0.00061 | 0.00433 | 0.00036 | 487 | 24.1 | 438.2 | 4.1 | 430.6 | 3.7 |
| 17 | 55.1 | 488.7 | 716.9 | 0.68 | 0.05516 | 0.00020 | 0.52571 | 0.00360 | 0.06910 | 0.00044 | 0.00261 | 0.00014 | 420 | 9.3 | 429.0 | 2.4 | 430.7 | 2.6 |
| 18 | 12.7 | 81.6 | 187.8 | 0.43 | 0.05523 | 0.00042 | 0.52585 | 0.00522 | 0.06909 | 0.00051 | 0.00444 | 0.00035 | 420 | 16.7 | 429.1 | 3.5 | 430.7 | 3.1 |
| 19 | 45.6 | 310.5 | 731.1 | 0.43 | 0.05524 | 0.00023 | 0.52610 | 0.00384 | 0.06912 | 0.00050 | 0.00291 | 0.00015 | 420 | 9.3 | 429.2 | 2.6 | 430.9 | 3.0 |
| 20 | 26.0 | 159.4 | 395.0 | 0.40 | 0.05501 | 0.00028 | 0.52363 | 0.00488 | 0.06900 | 0.00052 | 0.00343 | 0.00022 | 413 | 16.7 | 427.6 | 3.3 | 430.1 | 3.2 |
| 21 | 21.8 | 141.2 | 300.4 | 0.47 | 0.05552 | 0.00037 | 0.52779 | 0.00514 | 0.06911 | 0.00065 | 0.00348 | 0.00023 | 432 | 19.4 | 430.3 | 3.4 | 430.8 | 3.9 |
| 22 | 33.7 | 228.5 | 532.4 | 0.43 | 0.05541 | 0.00026 | 0.52626 | 0.00534 | 0.06897 | 0.00070 | 0.00291 | 0.00020 | 428 | 11.1 | 429.3 | 3.6 | 430.0 | 4.2 |
| 23 | 25.9 | 164.5 | 367.0 | 0.45 | 0.05601 | 0.00034 | 0.53303 | 0.00614 | 0.06907 | 0.00072 | 0.00342 | 0.00023 | 454 | 13.0 | 433.8 | 4.1 | 430.6 | 4.4 |
| 24 | 15.9 | 137.8 | 200.2 | 0.69 | 0.05534 | 0.00037 | 0.52539 | 0.00538 | 0.06887 | 0.00057 | 0.00310 | 0.00022 | 433 | 16.7 | 428.7 | 3.6 | 429.3 | 3.4 |
| 25 | 18.4 | 100.5 | 218.5 | 0.46 | 0.05532 | 0.00039 | 0.52574 | 0.00603 | 0.06894 | 0.00065 | 0.00472 | 0.00033 | 433 | 16.7 | 429.0 | 4.0 | 429.8 | 3.9 |
| 26 | 16.8 | 78.0 | 223.8 | 0.35 | 0.05551 | 0.00039 | 0.52769 | 0.00549 | 0.06908 | 0.00065 | 0.00519 | 0.00043 | 432 | 19.4 | 430.3 | 3.7 | 430.6 | 3.9 |
| 27 | 9.2 | 44.5 | 114.0 | 0.39 | 0.05557 | 0.00062 | 0.52771 | 0.00743 | 0.06899 | 0.00070 | 0.00783 | 0.00079 | 435 | 25.9 | 430.3 | 4.9 | 430.1 | 4.2 |

[1] Analysis numbers correspond to those in circles of Figure 5

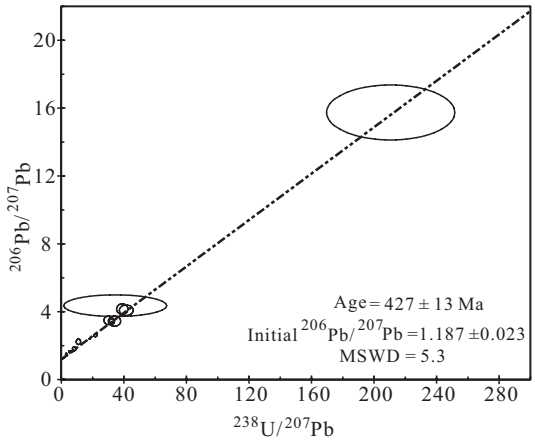


FIG. 7. $^{238}U/^{207}Pb$-$^{206}Pb/^{207}Pb$ isochron diagram for cassiterite from the Baiganhu district. Each point represents one grain.

(Table 3). The $\delta^{18}O_{H_2O}$ values of fluids are calculated using the quartz-water fractionation equation, $1{,}000\ ln\alpha_{Q\text{-}H_2O} = 3.38 \times (10^6/T^2) - 3.40$, of Clayton et al. (1972) and the average homogenization temperature (549.75 K) of fluid inclusions in quartz in the same stage as the sample. The calculated values range from +4.5 to +6.4‰. The measured $\delta D$ of fluids in inclusions varied from –65 to –43‰.

TABLE 2. U-Pb Isotope Data for Cassiterite from the Baiganhu Main Deposit (sample KK-21)

| $^{238}U/^{207}Pb$ | $2\sigma$ | $^{206}Pb/^{207}Pb$ | $2\sigma$ |
|---|---|---|---|
| 1.29 | 0.05 | 1.26 | 0.01 |
| 1.46 | 0.06 | 1.27 | 0.01 |
| 3.15 | 0.18 | 1.50 | 0.02 |
| 18.3 | 0.14 | 2.40 | 0.01 |
| 8.26 | 0.47 | 1.81 | 0.05 |
| 1.59 | 0.02 | 1.29 | 0.01 |
| 1.69 | 0.05 | 1.27 | 0.01 |
| 21.8 | 0.41 | 2.61 | 0.03 |
| 1.35 | 0.01 | 1.27 | 0.01 |
| 5.31 | 0.24 | 1.64 | 0.02 |
| 30.3 | 1.25 | 3.49 | 0.10 |
| 3.66 | 0.06 | 1.43 | 0.01 |
| 11.0 | 0.58 | 2.23 | 0.07 |
| 41.6 | 1.82 | 4.09 | 0.13 |
| 0.40 | 0.01 | 1.20 | 0.01 |
| 32.5 | 0.18 | 3.35 | 0.01 |
| 0.54 | 0.04 | 1.25 | 0.01 |
| 2.74 | 0.03 | 1.36 | 0.01 |
| 7.93 | 0.07 | 1.71 | 0.01 |
| 0.87 | 0.02 | 1.23 | 0.01 |
| 2.31 | 0.02 | 1.33 | 0.01 |
| 0.14 | 0.01 | 1.19 | 0.01 |
| 0.77 | 0.02 | 1.22 | 0.01 |
| 34.5 | 13.43 | 4.36 | 0.26 |
| 2.95 | 0.08 | 1.39 | 0.01 |
| 3.52 | 0.03 | 1.42 | 0.01 |
| 34.0 | 1.61 | 3.44 | 0.12 |
| 6.85 | 0.20 | 1.66 | 0.02 |
| 211 | 16.8 | 15.8 | 0.66 |
| 32.3 | 0.72 | 3.42 | 0.06 |
| 0.98 | 0.02 | 1.25 | 0.01 |
| 39.0 | 1.49 | 4.16 | 0.13 |

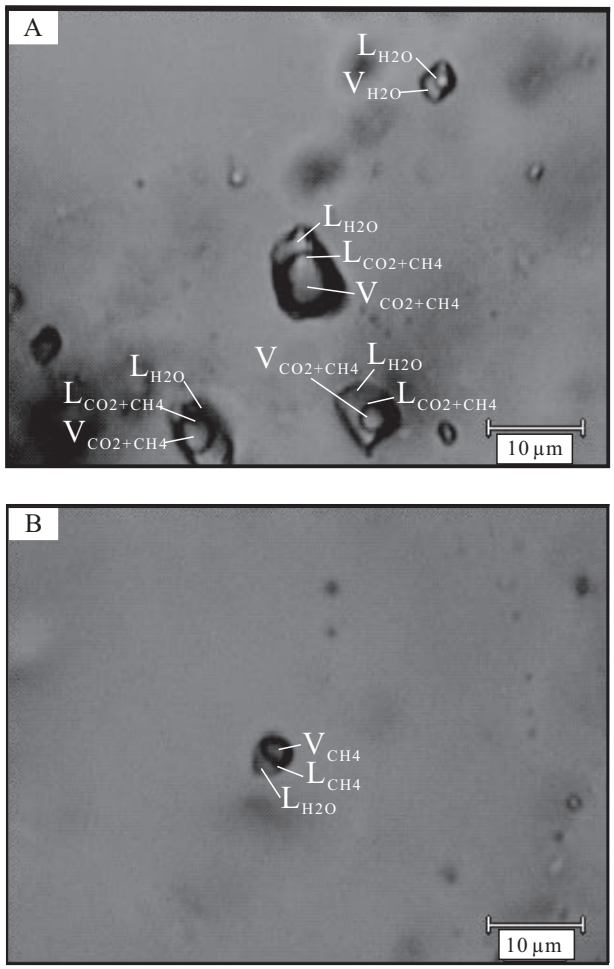


FIG. 8. Photomicrographs for the fluid inclusions in quartz from wolframite- and cassiterite-bearing E-W–trending quartz veins in the Baiganhu district. A. $CO_2$- and $CH_4$-bearing three-phase inclusions and liquid-rich two-phase aqueous inclusions in the Keke-Kaerde deposit. B. Inclusion containing almost pure $CH_4$ in the Bashi-Erxi deposit.

## Discussion

### *Age constraints on ore formation*

The U-Pb zircon age of 430.5 ± 1.2 Ma for the monzogranite is similar to the U-Pb zircon age of 432.3 ± 0.8 Ma for potassic granites (Shaanxi Geological Institute, unpub. data). The data indicate that granitoid magmatism in the Baiganhu W-Sn district occurred in the early Silurian period. This period corresponds to the end of subduction of the Proto-Tethyan Oceanic plate followed by local extension.

Cassiterite contains significant amounts of U and has an exceptional ability to retain both U and Pb which allows U-Pb dating (Yuan et al., 2011). This study yielded a U-Pb isochron age of 427 ± 13 Ma (Fig. 7). The age is essentially identical to that of the monzogranite within analytical uncertainties. The data confirms that the W-Sn mineralization was contemporaneous with intrusion of monzogranitic rocks in the area.

The Nanling region in southern China is the major W-Sn mining district in China. The mineralization took place in the Late Jurassic (160–150 Ma; Mao et al., 2007; Feng et al., 2011). The early Silurian W-Sn mineralization of the Baiganhu

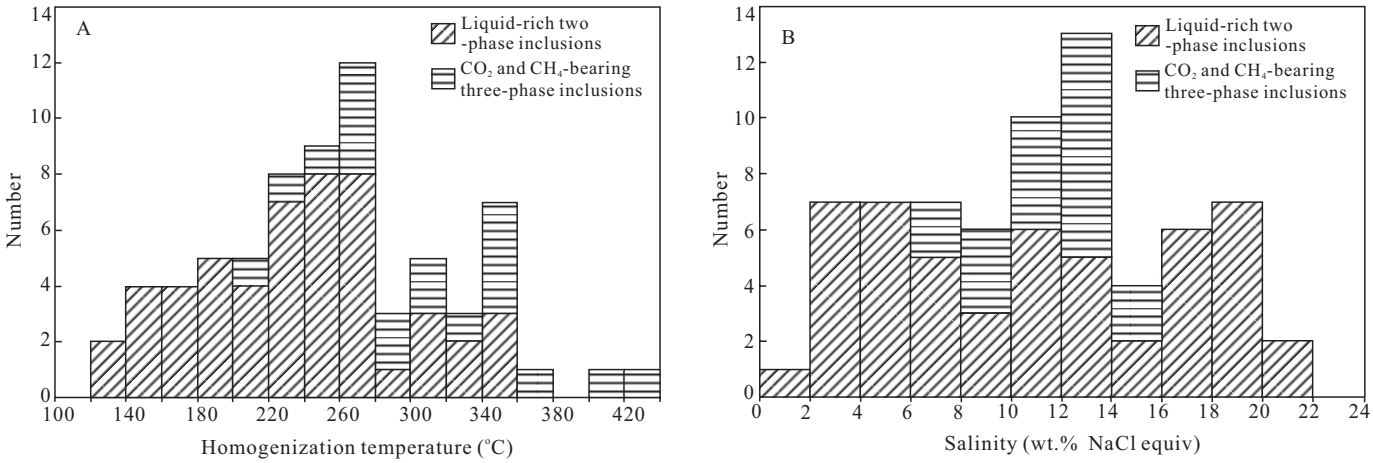


FIG. 9. Frequency histograms of homogenization temperatures (A, $n$ = 70) and salinities (B, $n$ = 70) for the fluid inclusions in quartz from wolframite- and cassiterite-bearing E-W–trending quartz veins in the Baiganhu district.

ore field suggests that the early Paleozoic is another important period for W-Sn mineralization in China. The mineralization belonging to this epoch in other regions includes the W mineralization at Xiaoliugou and Taergou (462 ± 13 Ma) and the W-Mo mineralization in the Qilian orogenic belt in northern China (Fig. 1A, Mao et al., 1999).

*Nature of vein-forming fluids*

There are two types of fluid inclusions in quartz of the wolframite- and cassiterite-bearing E-W–trending quartz veins. Aqueous fluid inclusions have filling temperatures ranging from 129° to 60°C, medium salinity (0.88–20.8 wt % NaCl equiv), and low density (0.72–1.06g/cm$^3$) with significant contents of $CO_2$. The second type, $CO_2$- and $CH_4$-bearing fluid inclusions, has filling temperatures ranging from 201° to 280°C, medium salinity (6.6–15.2 wt % NaCl equiv), and low density (0.60–0.91g/cm$^3$). The composition of fluids belongs to the NaCl-$H_2O$-$CO_2$ system with minor $CH_4$.

The aqueous two-phase inclusions coexist with $CO_2$-bearing three-phase inclusions (varying ratios of $CO_2$ to $H_2O$) in single quartz grains (Fig. 8A), suggesting immiscible separation of fluids during quartz crystallization. The presence of $CH_4$ in fluids likely promote the immiscibility of $CO_2$-rich and saline aqueous fluids at deeper levels (Naden and Shepherd, 1989). Fluid immiscibility is commonly accompanied by a sharp change in temperature and chemistry of fluids, which may result in metal precipitation in a variety of deposits, including W deposits (Higgins, 1985) and W-bearing polymetallic deposits (Seal et al., 1987; Polya, 1989).

The calculated $\delta^{18}O_{H_2O}$ of fluids and $\delta$D of inclusion fluids vary from +4.5 to +6.4‰ and –65 to –43‰, respectively, which plot in a confined area in the diagram of $\delta^{18}O_{H_2O}$-$\delta$D (Fig 10). They are within the field of magmatic water with no evidence of mixing with fluids from other sources, such as meteoric waters (Fig. 10). The data suggest that the mineralizing fluids were derived from monzogranite magmas. The results are consistent with the spatial relationship of the mineralization with monzogranites and similar ages between cassiterite and monzogranites. The Early Silurian granitic magmatism was essential for the formation of the Baiganhu W-Sn deposits.

TABLE 3. Oxygen Isotope Compositions for Quartz and Hydrogen Isotope Compositions for Fluid Inclusions in Quartz of Wolframite- and Cassiterite-Bearing E-W–Trending Quartz Veins from the Baiganhu Tungsten-Tin District

| Orefield | Sample no.[1] | Fluid inclusion $\delta D_{V\text{-}SMOW}$(‰) | Quartz $\delta^{18}O_{V\text{-}SMOW}$(‰) | Fluid[2] $\delta^{18}O_{H2O}$(‰) |
|---|---|---|---|---|
| Keke-Kaerde | KK-9 | –62 | 13.6 | 5.8 |
| | KK-10 | –44 | 13.6 | 5.8 |
| | KK-11 | –43 | 13.9 | 6.1 |
| | KK-12 | –49 | 14.0 | 6.2 |
| | KK-13 | –47 | 12.6 | 4.8 |
| | KK-14 | –53 | 12.3 | 4.5 |
| Bashi-Erxi | BE-15 | –59 | 14.2 | 6.4 |
| | BE-16 | –57 | 13.3 | 5.5 |
| | BE-17 | –59 | 13.3 | 5.5 |
| | BE-18 | –57 | 12.3 | 4.5 |
| | BE-19 | –65 | 13.7 | 5.9 |

[1] Sample locations are shown in Figure 1C and E

[2] The $\delta^{18}O_{H_2O}$ was calculated using the fractionation equation 1,000 $ln\alpha_{Q\text{-}H_2O} \approx 3.38 \times (10^6/T^2) - 3.40$ (Clayton et al., 1972), where T is 549.75 K, the average homogenization temperature of fluid inclusions

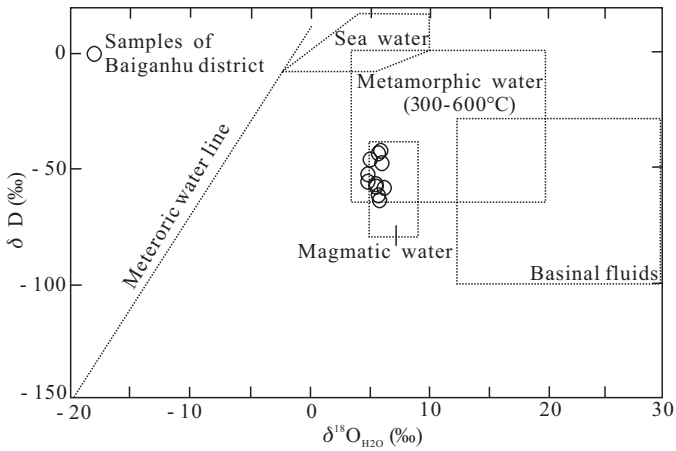


FIG. 10. Hydrogen isotope compositions of fluids in inclusions of quartz and oxygen isotope composition for fluids calculated from $\delta^{18}O$ values of quartz in wolframite- and cassiterite-bearing E-W–trending quartz veins from the Baiganhu district. Fields for waters of different origins are from Taylor (1997).

*Tungsten-tin mineralization in the Baiganhu district*

Unaltered monzogranites in the Baiganhu area contain high contents of W (avg 20.5 ppm, $n = 30$) and Sn (avg 9.4 ppm, $n = 30$; Li et al., 2006). The values may be compared to the crustal averages of 1 ppm W and 2.5 ppm Sn (Taylor and McLennan, 1985). The data suggest that the parental magmas for the monzogranites likely contained high W and Sn. Magmatic fluids separated from such granitic magmas are enriched in W and Sn (Webster et al., 2004).

In summary, the most likely sequence of events is described below. The cessation of subduction and local extension in the area allowed a large scale of magmatic event in the early Paleozoic. Magmatic fluids were separated from the parental magmas and reacted with the country rock limestone, forming skarns and crystallizing scheelite. Shortly after skarn formation, greisens developed in the upper parts of monzogranite intrusions and in the country rock, and scheelite and wolframite crystallized in the greisens. This was followed by the formation of wolframite- and cassiterite-bearing E-W–trending quartz veins within the muscovite-bearing zone of monzogranite and skarns. The fluids moving along fractures were overpressured with significant $CO_2$ and $CH_4$, producing breccias around and within veins. Decreasing pressures and temperature likely caused fluid immiscibility into $CO_2$-rich and saline aqueous fluids when the fluid ascents along the fractures. This further prompted the crystallization of W and Sn minerals and quartz. Later, chalcopyrite-bearing NE-SW–trending quartz veins formed.

## Conclusions

1. The W-Sn mineralization of the Baiganhu district is divided into three stages: (I) scheelite-bearing skarn stage, (II) wolframite- and scheelite-bearing greisenization stage, and (III) wolframite- and cassiterite-bearing E-W–trending quartz vein stage.

2. The U-Pb ages of zircon suggest that monzogranite intruded at 430.5 ± 1.2 Ma. The $^{206}Pb/^{207}Pb$-$^{238}U/^{207}Pb$ isochron age, 427 ± 13 Ma, of cassiterite confirms that the mineralization was synchronous with the intrusion of monzogranite in the Early Silurian period, shortly after cessation of the subduction of the Proto-Tethean Ocean.

3. Quartz from wolframite- and cassiterite-bearing quartz veins has $\delta^{18}O_{SMOW}$ ranging from +12.3 to +14.2‰. The values of $\delta^{18}O_{H_2O}$ calculated for the mineralizing fluids vary from +4.5 to +6.4‰. The $\delta D$ values for inclusion fluids range from –65 to –43‰. These data support a model whereby the mineralization took place from fluids from monzogranite magmas.

4. Fluid inclusions have moderate salinity (10–14 wt % NaCl equiv), low density (0.60–1.06 g/cm$^3$), and moderate homogenization temperatures (240°–270°C). Aqueous inclusions coexist with $CO_2$- and $CH_4$-rich inclusions. The data suggest immiscible separation of fluids likely led to W-Sn mineralization of the quartz vein-type deposits.

## Acknowledgments

We thank A.S. Zhou, Z.K. Wang, S. Wang, B. Zhang, K. Li, B. Qian, J.W. Zhang, and Y.L. Wang for their help during our field works. We also thank H.J. Gong at Northwest University, K.J. Hou at Chinese Academy of Geosciences, Z.H. Wang and M.F. Ye at Xi'an Institute of Geology and Mineral Resources, H.K. Li at Tianjin Institute of Geology and Mineral Resources, and H.B. Liu at Beijing Research Institute of Uranium Geology for their help in sample determination and data processing. We are grateful to F. Ye, H. Li, H.Q. Yang, and X.Y. Xu at Xi'an Institute of Geology and Mineral Resources, for their valuable suggestions that helped to improve an early manuscript of this paper. This research was financially supported by a grant from Natural Science Foundation of China (41102050), Natural Science Basic Research Plan in Shaanxi Province of China (2013JM5010), project from the National Science and Technology Pillar Program during the Eleventh Five-Year Plan period (2006BAB01A01), and projects from China Geological Survey (1212011121088, 1212011121092, 1212011120183).

## REFERENCES

Carlin, J.F., Jr., 2013, Tin: U.S. Geological Survey Minerals Yearbook 2011, p. 77.01–77.10.

Clayton, R.N., O'Neil, J.R., and Mayeda, T.K., 1972, Oxygen isotope exchange between quartz and water: Journal of Geophysical Research, v. 77, p. 3057–3067.

Coleman, M.L., Sheppard, T.J., Durham, J.J., Rouse, J.E., and Moore, G.R., 1982, Reduction of water with zinc for hydrogen isotope analysis: Analytical Chemistry, v. 54, p. 993–995.

Feng C.Y., Zeng Z.L., Zhang D.Q., Qu W.J., Du A.D, Li D.X., and She H.Q., 2011, SHRIMP zircon U-Pb and molybdenite Re-Os isotopic dating of the tungsten deposits in the Tianmenshan-Hongtaoling W-Sn orefield, southern Jiangxi Province, China, and geological implications: Ore Geology Reviews, v. 43, p. 8–25.

Gao, Y.B., Li, W.Y., and Tan, W.J., 2010, Metallogenic characteristics and analysis of the prospecting potential in the area of Qimantage: Northwestern Geology, v. 43, p. 35–42 (in Chinese with English abs.).

Higgins, N.C., 1985, Wolframite deposition in a hydrothermal vein systerm: the Grey River tungsten prospect, Newfoundland, Canada: Economic Geology, v. 80, p. 1297–1327.

Hou, K.J., Li, Y.H., and Tian, Y.R., 2009, In situ U-Pb zircon dating using laser ablation-multi ion counting-ICP-MS: Mineral Deposits, v. 28, p. 481–492 (in Chinese with English abs.).

Jiang, Y.H., Liao, S.Y., Yang, W.Z., and Shen, W.Z., 2008, An island arc origin of plagiogranites at Oytag, western Kunlun orogen, northwest China: SHRIMP zircon U-Pb chronology, elemental and Sr-Nd-Hf isotopic geochemistry and Paleozoic tectonic implications: Lithos, v. 106, p. 323–335.

Li, D.P., Li, J., Zhang, H.J, Li, X.L., Zhou, X.K., and Du, S.X., 2003, The turbidite of the Silurian Baiganhu formation in the Qimantage Mountain, eastern Kunlun: Geology of Shaanxi, v. 21, p. 39–44 (in Chinese with English abs.).

Li, H.M., Shi, Y.D., Liu, Z., Wang, B.J., Wang, Z.L., and Qiu, X.P., 2006, Geological features and origin of the Baigan Lake W-Sn deposit in the Ruoqiang area, east Kunlun Mountains, China: Geological Bulletin of China, v. 25, p. 277–281 (in Chinese with English abs.).

Li, R.S., Ji, W.H., and Yang, Y.C., 2008, The geology in Kunlun and its adjacent region: Beijing, Geological Publishing House, 400 p. (in Chinese).

Liu, G.Z., Li, H.M., Wang, J.S., Zhang, T.M., and Song, C.Y., 2007, Mineralized body model of the tungsten and tin ore field in Baiganhu, eastern Kunlun, Xinjiang: Xinjiang Geology, v. 25, p. 169–173 (in Chinese with English abs.).

Liu, Y.S., Gao, S., Hu, Z.C., Gao, C.G., Zong, K.Q., and Wang, D.B., 2010, Continental and oceanic crust recycling-induced melt-peridotite interactions in the Trans-North China progen: U-Pb dating, Hf isotopes and trace elements in zircons from mantle xenoliths: Journal of Petrology, v. 51, p. 537–571.

Liu, Z.F., Cui, Y.R., and Wei, W., 2007, The geochemical characteristics of the Baiganhu W-Sn deposit, Dongkunlun, Xinjiang: Jilin Geology, v. 26, p. 54–60 (in Chinese with English abs.).

Ludwig, K.R., 2003, Isoplot/EX, Version 3. A geochronological toolkit for Microsoft Excel: Berkeley Geochronology Center Special Publications, 4 p.

Mao, J.W., Zhang, Z.H., Zhang, Z.C., Yang, J.M., Wang, Z.L., and Du, A.D., 1999, Re-Os age dating of molybdenites in the Xiaoliugou tungsten deposit in the northern Qilian Mountains and its significance: Geological Review, v. 45, p. 412–416 (in Chinese with English abs.).

Mao, J.W., Xie, G.Q., Guo, C.L., and Chen, Y.C., 2007, Large-scale tungsten-tin mineralization in the Nanling region, South China: Matallogenic ages and corresponding geodynamic processes: Acta Petrologica Sinica, v. 23, p. 2329–2338 (in Chinese with English abs.).

Mo, X.X., Luo, Z.H., Deng, J.F., Yu, X.H., Liu, C.D., Chen, H.W., Yuan, W.M., and Liu, Y.H., 2007, Granitoids and crustal growth in the east Kunlun orogenic belt: Geological Journal of China Universities, v. 13, p. 403–414 (in Chinese with English abs.).

Naden, J., and Shepherd, T.J., 1989, Role of methane and carbon dioxide in gold deposition: Nature, v. 342, p. 793–795.

Pan, Y.S., Wang,Y., Matte, Ph., and Tapponnier, P., 1994, Tectonic evolution along the geotraverse from Ye Cheng to Shi quan he: Acta Geologica Sinica, v. 68, p. 295–307 (in Chinese with English abs.).

Polya, D.A., 1989, Chemistry of the main-stage ore-forming fluids of the Panasqueira W-Cu(Ag)-Sn deposit, Portugal: Implications for models of ore genesis: Economic Geology, v. 84, p. 1134–1152.

Seal, R.R., II., Clark, A.H., and Morrissy, C.J., 1987, Stockwork tungsten (scheelite)-molybdenum mineralization, Lake George, southwestern New Brunswick: Economic Geology, v. 82, p. 1259–1282.

Shedd, K.B., 2013, Tungsten, 2011: U.S. Geological Survey Minerals Year Book, p. 79.01–79.20.

Slama, J., Kosler, J., Condon, D.J., Crowley, J.L., Gerdes, A., Hanchar, J.M., Horstwood, M.S.A., Morris, G.A., Nasdala, L., Norberg, N., Schaltegger, U., Schoene, B., Tubrett, M.N., and Whitehouse, M.J., 2008, Plesovice zircon: A new natural reference material for U-Pb and Hf isotopic microanalysis: Chemical Geology, v. 249, p. 1–35.

Song, M.D., Liu, Z., Li, H.M., and Sun X.Y., 2010, Geological background and potentiality analysis of Baiganhu metallogenic belt in east Kunlun, Xinjiang: Northwestern Geology, v. 43, p. 44–51 (in Chinese with English abs.).

Taylor, H.P., Jr., 1997, Oxygen and hydrogen isotope relationships in hydrothermal deposits, *in* Barnes, H.L., ed., Geochemistry of hydrothermal deposits, 3rd ed.: New York, John Wiley and Sons, p. 229–302.

Taylor, S.R., and McLennan, S.M., 1985, The continental crust: Its composition and evolution: Oxford, Blackwell Scientific Publication, 312 p.

Webster, J.D., Thomas, R., Forster, H-J., Seltmann, R., and Tappen, C., 2004, Geochemical evolution of halogen-enriched granite magmas and mineralizing fluids of the Zinnwald tin-tungsten mining district, Erzgebirge, Germany: Mineralium Deposita, v. 39, p. 452–472.

Yang, J.S., Robinson, P.T., Jiang, C.F., and Xu, Z.Q., 1996, Ophiolites of the Kunlun Mountains, China and their tectonic implications: Tectonophysics, v. 258, p. 215–231.

Yang, J.S., Shi, R.D., Wu, C.L., Wang, X.B., and Robinson, P.T., 2009, Dur'ngoi ophiolite in east Kunlun, northeast Tibetan plateau: Evidence for Paleo-Tethyan suture in northwest China: Journal of Earth Science, v. 20, p. 303–331.

Yuan, S.D., Peng, J.T., Hao, S., Li, H.M., Geng, J.Z., and Zhang, D.L., 2011, In situ LA-MC-ICP-MS and ID-TIMS U-Pb geochronology of cassiterite in the giant Furong tin deposit, Hunan Province, south China: New constraints on the timing of tin-polymetallic mineralization: Ore Geology Reviews, v. 43, p. 235–242.